1
2
3

# Fast, multicolor 3-D imaging of brain organoids with a new single-objective two-photon virtual light-sheet microscope*

Irina Rakotoson,[1,2,3,4+] Brigitte Delhomme,[1,2,3+] Philippe Djian,[1,2,3+] Andreas Deeg,[5] Maia Brunstein,[1,2,3] Christian Seebacher,[5] Rainer Uhl,[5] Clément Ricard,[1,2,3,§] and Martin Oheim[1,2,3,§,✉]

[1]CNRS UMR 8118, Brain Physiology Laboratory, Paris F-75006, France
[2]Fédération de Recherche en Neurosciences CNRS FR 3636, Paris F-75006, France
[3]Faculté de Sciences Fondamentales et Biomédicales, Université Paris Descartes, PRES Sorbonne Paris Cité, F-75006 Paris, France
[4]Master programme: BCPP (Biologie cellulaire physiologie et pathologie), spécialité Neurosciences
[5]TILL.id, Am Klopferspitz 19, D-82153 Planegg/Martinsried, Munich, Germany

*corresponding author

Martin Oheim
martin.oheim@parisdescartes.fr

+co-first authors
§co-last authors

*Elements of this work has been published in the Master thesis of I.R. [1]

## ABSTRACT

Human inducible pluripotent stem cells (hiPSCs) hold a large potential for disease modeling. hiPSC-derived human astrocyte and neuronal cultures permit investigations of neural signaling pathways with subcellular resolution. Combinatorial cultures, and three-dimensional (3-D) embryonic bodies enlarge the scope of investigations to multi-cellular phenomena. A the highest level of complexity, brain organoids that – in many aspects – recapitulate anatomical and functional features of the developing brain permit the study of developmental and morphological aspects of human disease. An ideal microscope for 3-D tissue imaging at these different scales would combine features from both confocal laser-scanning and light-sheet microscopes: a micrometric optical sectioning capacity and sub-micrometric spatial resolution, a large field of view and high frame rate, and a low degree of invasiveness, i.e., ideally, a better photon efficiency than that of a confocal microscope. In the present work, we describe such an instrument that belongs to the class of two-photon (2P) light-sheet microsocpes. Its particularity is that – unlike existing two- or three-lens designs – it is using a single, low-magnification, high-numerical aperture objective for the generation and scanning of a virtual light sheet. The microscope builds on a modified Nipkow-Petráň spinning-disk scheme for achieving wide-field excitation. However, unlike the common Yokogawa design that uses a tandem disk, our concept combines micro lenses, dichroic mirrors and detection pinholes on a single disk. This design, advantageous for 2P excitation circumvents problems arising with the tandem disk from the large wavelength-difference between the infrared excitation light and visible fluorescence. 2P fluorescence excited in by the light sheet is collected by the same objective and imaged onto a fast sCMOS camera. We demonstrate three-dimensional imaging of TO-PRO3-stained embryonic bodies and of brain organoids, under control conditions and after rapid (partial) transparisation with triethanolamine and *f*ormamide (RTF) and compare the performance of our instrument to that of a confocal microscope having a similar numerical aperture. 2P-virtual light-sheet microscopy permits one order of magnitude faster imaging, affords less photobleaching and permits better depth penetration than a confocal microscope with similar spatial resolution.

(333 words, 350 possible)

77   **INTRODUCTION**

78

79   The development of pharmacological treatments for neuropsychiatric and neurodegenerative

80   diseases has been hampered by the poor availability of preclinical models that adequately

81   capture the complexity of human disorders [2].

82      Human inducible pluripotent stem cells (hIPSCs) offer a promising platform for disease

83   modeling and drug screening. A comparably new technique is the directed differentiation and

84   reprogramming of patient fibroblasts into neurons, astrocytes, microglia and oligodendro-

85   cytes. Their combinational culture permits the growth of embryonic bodies (EBs) and brain

86   organoids, 3-D cultures that – in many aspects – recapitulate the development of the human

87   brain [3; 4]. Together, hIPSCs, EBs, and brain organoids enable observations and experiments

88   that were previously inconceivable, neither on human subjects, nor in animal models [5; 6].

89   Recent reports of functional, fully vascularized brain organoids have spurred hopes of

90   growing even larger 3-D cell assemblies [7], bringing the hitherto theoretical '*brain in a vat*'[1]

91   within reach of the imaginable.

92      Elucidation of neural circuit (dys-)function would benefit from the detailed, 3-D

93   visualization of the fine structure of neurons, astrocytes and blood vessels over large fields of

94   view and deep in tissue. Large-scale neuroanatomical imaging has become possible in cleared

95   tissue sections [8], brain organoids [9] or even entire brains [10], but in many cases the

96   resolution is rather at level of cell bodies that at the synaptic scale. In addition to the diffi-

97   culties associated with transparisation and tissue shrinking, imaging of large tissue volumes at

98   spatial high-resolution presents considerable challenges: confocal and two-photon (2P) laser

99   scanning microscopies set the 'gold-standard' for diffraction-limited fluorescence imaging,

100   but – being in most of their implementations point-scanning, i.e., sequential techniques – the

---

[1] The '*brain in a vat*' or '*brain in a jar*' is a is a scenario used in a variety of *Gedankenexperiments* intended to draw out certain features of human conceptions of knowledge, reality, truth, mind, consciousness and meaning. It is an updated version of René Descartes' evil demon thought experiment. It has been extensively used by Hilary Putnam (*Reason, Truth and History,* 1981), in an argument inspired from Roald Dahl's short story, « *William and Mary* » (1959).

101    image acquisition is often painstakingly slow. Particularly, the reconstruction of large

102    volumes often requires hours if not days of recording, putting high demands on mechanical

103    stability of the microscope, photostablity of the used fluorescent dyes, and incurring conside-

104    rable cost for beam time. Line- and multi-spot scanning schemes overcome these limitations

105    by parallelizing the *excitation*, but they trade off resolution against speed and they often have

106    relatively small fields of view, requiring image stitching for larger fields.

107        On the other end, selective-plane illumination microscopes (SPIM) [11] or light-sheet

108    microscopes [12] decouple fluorescence excitation and collection by using orthogonal

109    illumination and detection optical paths. Light-sheet microscopes have established themselves

110    as efficient workhorses for volume imaging in cleared tissue. It is the parallelization of *both*

111    *excitation* and fluorescence *detection* that allows for rapid 3-D imaging on these instruments

112    [13; 14]. However, one consequence of the lower-NA illumination and a result of excitation-

113    light scattering in not perfectly transparent samples, is that the axial resolution of light-sheet

114    microscopes remains poor compared to the optical sectioning achieved by spot-scanning

115    microscopes. Improvement has been made with 2P light-sheet excitation [15; 16], by

116    combining 2P-line excitation and confocal slit detection [17], by the use of Airy- [18] or

117    Bessel-beams for excitation [19; 20; 21], or a combination of these techniques [22; 23].

118    However, many of these recent techniques are not yet commercial and they afford

119    considerable cost and complexity compared to standard 1- and 2P-laser scanning micro-

120    scopes.

121        Another limitation of light sheet microscopes results from their orthogonal arrangement of

122    excitation and collection objectives: the need for non-standard procedures for embedding and

123    holding the sample. Variants of light-sheet microscopes in which both illumination and

124    detection objectives are mounted at an oblique angle with respect to the tissue surface and the

125    sample half space is left free exist [24; 25; 26], but they have remained comparably marginal.

126    An ideal microscope for volume imaging in cleared brain tissue [27] would combine

127    speed, a sub-µm lateral and µm-axial resolution, a mm-field of view, an excitation depth of a

128    few mm, a certain robustness to imperfect sample transparisation and a large free space under

129    the objective.

130    Here, we present a microscope with excitation- and detection-parallelization that gets

131    close to this ideal by combining advantages of 2P laser-scanning and light-sheet techniques.

132    Our <u>On</u>-<u>a</u>xis 2-photon light-<u>s</u>heet generation *in-vivo* <u>i</u>maging <u>s</u>ystem (OASIS) uses a vast

133    array of micro lenses arranged in four nested spirals on a single spinning disk to

134    simultaneously scan ~40 independent excitation spots in the focal plane of a single, long-

135    working distance, low-magnification, high-NA objective [28]. Rotation of the disk at 5,000

136    rpm results in rapid multi-spot scanning and creates a virtual light sheet in the focal plane of

137    the objective. The fluorescence generated in each of the excitation spots is imaged through

138    the same objective onto a pinhole in the center of each micro lens. With the remainder of the

139    lens made opaque to (scattered) fluorescence by a dichroic coating sparing only the tiny

140    pinhole, only fluorescence emanating from the focus is detected. Each pinhole is imaged onto

141    a large-format scientific Complementary Metal Oxide Semiconductor (sCMOS) camera,

142    allowing near-diffraction limited imaging over a large field of view. This patented optical

143    design, combining micro-lenses and perforated dichroic mirrors on a single-spinning disk,

144    allowed us to retain the in-line, single-objective geometry of a classical microscope without

145    the requirement for orthogonal illumination. As a consequence, our OASIS microscope is

146    more versatile than two- or three-objective light-sheet microscopes. With its compact

147    footprint (43 cm by 12 cm, or 17" × 5"), it can accommodate large samples (cells, slices,

148    explants and entire animals, *in vivo*) without requiring tedious mounting procedures or special

149    sample holders. The OASIS concept combines the optical sectioning, spatial resolution and

150    field-of-view of a 2P-scanning microscope with the speed of a light-sheet microscope. Due to

151  2P excitation, out-of-focus fluorescence excitation, photo-bleaching and photo-damage are

152  much reduced compared to a classical confocal microscope. We here describe this new

153  microscope and compare it to a confocal laser-scanning microscope (CLSM) for imaging

154  clarified brain organoids with nuclear staining.

155
156
157
158  **RESULTS AND DISCUSSION**
159

160  **Wide-field two-photon microscopy at diffraction-limited resolution**

161  With our <u>O</u>n-<u>a</u>xis 2-photon light-<u>s</u>heet generation *in-vivo* <u>i</u>maging <u>s</u>ystem (OASIS), we retain

162  the in-line geometry of a classical upright microscope with a single objective lens. We

163  introduce a novel spinning-disk concept, rethought and specifically designed for wide-field 2P

164  microscopy, **Fig. 1***A*. Briefly, the expanded and shaped beam of a fs-pulsed infrared laser is

165  focused by an array of micro lenses to produce some 40 evenly lit excitation spots. These

166  spots are imaged by the tube lens and objective into the sample plane where they are each

167  spaced, on average, by 28 µm, **Fig. 1***A*, *inset* ❶.  A total of almost 5,000 micro lenses are

168  arranged in four nested spirals that scan these spots upon rotation of the disk. At 5,000 rpm

169  (i.e., one turn every 12 ms, much shorter than camera integration times used here) the multi-

170  spot scanning generates a virtual light sheet permitting wide-field, direct-view 2P imaging.

171  Unlike earlier 2P-spinning disk microscopes [29; 30; 31] that were based on modified

172  Yokogawa-type spinning-disk confocal microscopes, we use a different disk geometry. Where

173  the Yokogawa dual-disk design requires two disks, one with micro lenses, the other one with

174  confocal pinholes, the OASIS microscope relies on a single disk on which micro lenses and

175  pinholes that are arranged on the different faces of the same optical element. Specifically, we

176  do not use an extra dichroic, but each micro lens comes with its own dichroic mirror; the

177  dielectric coating is omitted over a central circular aperture of 60-µm diameter. The use of a

178  single disk is advantageous in view of the large wavelength difference between the near-

179    infrared excitation and the visible fluorescence, which had previously reduced the efficiency

180    of 2P-spinning disk miroscopes. However, this simplification comes at a price as it required a

181    complete re-design of the microscope optical path. On the excitation side, the micro lenses

182    must be uniformly illuminated with a collimated fs-pulsed IR laser beam to generate an array

183    of focused spots. On the collection side, to pass the pinholes, the detected fluorescence must

184    arrive focused at the level of the pinholes. The required optical path-length difference be-

185    tween excitation and emission light is achieved by introducing a corrective distance element

186    in the non-infinity space: while the longer-wavelength excitation light passes straight through

187    the device, the shorter-wavelength fluorescence takes a detour and travels a longer path to

188    produce the desired focal offset, *inset* ❷. This patented optical scheme critically relies

189    extremely flat shallow-incidence long-pass dichroic mirrors to preserve the phase front of the

190    beam and maintain the optical resolution.

191         The 2P-excited fluorescence generated in each of the spots is collected through the

192    same objective and imaged onto the tiny pinholes in the dichroic coating of the microlenss

193    (**Fig. 1***A*, *inset* ❷). Relay optics then images these pinholes onto a large-format sCMOS

194    camera. The resulting pixel size in the sample plane is 182 nm, within the Nyquist limit.

195         This detection is partially confocal (the 60-µm pinhole diameter correspond to a con-

196    focal aperture of 2 Airy units), so that only ballistic and snake-like photons but not scattered

197    fluorescence contribute to the signal, as illustrated by the exponential fluorescence drop with

198    increasing sample turbidity. Yet, as a result of the longer wavelength of excitation light, the

199    signal drop observed with the OASIS microscope was only half of that observed with a 1-P

200    CLSM at 633-nm excitation, **Fig. 1***B*. We can attribute the improved depth penetration of the

201    OASIS uniquely to excitation effects, because stopping down the confocal pinhole from 2 to 1

202    Airy units did not measurably alter the fluorescence decay on the CLSM.

203      With its small footprint (43 cm by 12 cm) and 22-cm clearance under the objective,

204      the OASIS microscope offers facile access and ample space around the objective, making it

205      an ideal platform for imaging large samples, but also for placing electrodes, application

206      pipettes or external fibers for photostimulation or photochemical uncaging, **Fig. 1***C*. Also, as a

207      re-sult of the large chip format of the sCMOS detector, we could implement simultaneous

208      dual-color detection by way of a custom image splitter, **Fig. S1**.

209      With the ×4.6 beam expander and a ×25/NA1.1w low-mag high numerical aperture

210      (NA) dipping objective [28], the OASIS microscope features a field of view with a 200 μm

211      image diagonal. A 5- to 6-fold larger field, making full use of the nominal field-of-view of the

212      same objective would be possible, but it requires more micro-lenses to be illuminated, which

213      in turn requires a more powerful laser than ours.

214      As a wide-field imaging system, the OASIS microscope simultaneously offers a fast

215      frame rate, a large field of view and it resolves tiny subcellular detail. We illustrate the sub-

216      micrometric resolution by imaging the fine tip of a spine from an autofluorescent pollen grain,

217      a typical test sample for 2P-microscopes, **Fig. 1***D*.

218      For estimating the optical sectioning capability of our OASIS microscope, we recor-

219      ded the axial ($z$-) intensity profile from a green fluorescent Chroma test slide and we quanti-

220      fied the $z$-resolution ($\Delta z$) by the full-width at half maximum (FWHM) of a Gaussian fitted

221      with the derivative of the $z$-profile [32], **Fig. 1***E*. Repeating the same experiment on a ZEISS

222      LSM710 demosntrates that OASIS offered a 1.3-fold better optical sectioning than the

223      confocal laser-scanning microscope (with the pinhole diameter set to 2 Airy diameter and

224      with a dipping objective having a similar NA, 1.1w vs. 1.0w; $\Delta z_{OASIS} = 2.75 \pm 0.02$ μm vs.

225      $\Delta z_{CLSM, 2Airy} = 3.47 \pm 0.02$ μm). In fact, its optical sectioning is close to that of a CLSM with

226      the pinhole stopped down to 1 Airy diameter ($\Delta z_{CLSM, 1Airy} = 2.55 \pm 0.02$ μm), **Fig. S2**.

227   The acquisition speed will be in practice be limited by the available signal, but the

228   theoretical minimal exposure time is bounded by the Nyquist limit, i.e., the time required for

229   two full rotations of the spiral on the disk. With a rotation time of 12 ms at 5,000 rpm and

230   four nested spirals, the minimal theoretical exposure time is 3 ms, i.e., 6 ms when taking into

231   account Nyquist's sampling theorem. Integration times should be multiples of 6 ms for

232   obtaining a homogeneously lit field of view. With the 100-fs pulses and mW average laser

233   power, $<P>$, per illumination spot used here, typical exposure times were of the order of

234   hundred ms, full frame, more than one order of magnitude faster than typical time required a

235   similarly resolved image with a 2P-scanning microscope.

236   Taken together, our OASIS virtual 2P light-sheet microscope offers better depth pene-

237   tration, a similar if not better spatial resolution and a considerably higher speed than a

238   conventional CSLM.

239   (figure 1 close to here)
240
241
242
243   **RTF-cleared TO-PRO3-labeled embryos as a test sample for 1- and 2P microscopies**
244
245   Next, we evaluated the performance of the OASIS microscope for 3-D imaging of partially

246   cleared brain tissue. We sought for a stereotypic, sparsely but homogenously labeled and thick

247   sample. To allow for a direct comparison between 1P-CLSM and our 2P virtual-light sheet

248   microscope, this labeling needed to be suitable for both linear- and non-linear excitation. To

249   minimize scattering and improve the depth penetration, we searched for a red-exciting, deep-

250   red emitting fluorophore. With these constraints in mind we opted for the nuclear stains TO-

251   PRO3 and Methyl Green (MG), having 1P-fluorescence excitation/emission maxima of

252   642/661 nm [33]) and 632/650 nm [34], respectively.

253   During preliminary experiments in 7-µm thin sections of a fixed (E14.5) mouse

254   embryo, we found TO-PRO3 fluorescence to be 2.1-fold brighter than that of MG upon 633-

255     nm excitation. We observed an even larger intensity ratio (×5.5) upon 2P-excitation at 760

256     nm, **Fig. 2***A*. Although non-linear excitation of TO-PRO3 at 1,100 nm has been reported [35;

257     36] we measured the 2P-action spectra and found peak excitations at 760 and 750 nm for TO-

258     PRO3 and MG, respectively, **Fig. 2***B*. Compared to the reported 1,100-nm excitation these

259     shorter wavelengths are within the tuning range of the standard Ti:Saphh laser and they

260     minimize thermal damage from near-infrared absorption and focal heating [37], a particular

261     concern for the multi-spot excitation scheme used here.

262     We next optimized the tissue transparisation procedure. Among the available methods

263     (see [38] for review), we focused on TDE [39], Clear$^{T2}$ [40] and RTF clearing [41]. The

264     rationale was that these methods require only short clearing episodes and they use solvents

265     compatible with dipping objectives. Mouse embryos were most transparent with TDE (60%),

266     followed by RTF and, by far, Clear$^{T2}$, for which the tissue was even more opaque than the

267     non-cleared control (probably due to volume shrinkage), **Fig. 2***C*.

268     In clearing, transparency is one issue, fluorescence preservation another. Depending

269     on the very method used, the observed signal loss was dramatic, with a 99.9% and 92%

270     attenuation of TO-PRO3 fluorescence following Clear$^{T2}$ and RTF clearing, respectively, **Fig.**

271     **2***D*. Increasing the laser power by a factor of 20 allowed us to acquire confocal images of TO-

272     PRO3 stained nuclei in slices of RTF-cleared embryos, **Fig. 2***E*, whereas TDE clearing

273     attenuated the fluorescence to undetectable levels, **Fig. S3**. To develop an order-of-magnitude

274     idea of the laser powers required for obtaining similar signal-to-noise levels with the OASIS

275     and CSLM, we finally compared images acquired upon 1- (at 633 nm) and 2-excitation (at

276     760 nm) of TO-PRO3 labeled nuclei in a thin section of RTF cleared mouse embryo. With a

277     confocal aperture of 2 Airy, we found a factor of ×4,000 btween linear and non-linear

278     excitation (2 µW vs. 8 mW/spot, respectively).

279    Based on these results, we decided to combine TO-PRO3 nuclear staining and RTF

280    clearing for directly comparing the performance of confocal and OASIS microscopes.

281
282    (figure 2 close to here)
283
284
285
286    **Faster and less invasive acquisition of 3-D image stacks**
287

288    Tracing fluorescent dendrites and axons to study the projections and connectivity in small

289    cellular net-works is a major goal of current neuroanatomy. At 250-nm lateral and

290    micrometric axial sampling and with typical pixel dwell times of 1 (10 µs), sequential single-

291    spot scanning schemes are necessarily slow, requiring  4 (40) ms, 4 (40) s and more than 1

292    (10) hrs for the acquisition of 3-D image stacks from cubes of 10 µm, 100 µm and 1 mm side-

293    length, respectively. Parallelizing both the excitation and emission detection, as with our

294    OASIS microscope is expected to considerably speed up the imaging of such large data sets.

295    Using TO-PRO3 nuclear staining as a proxy, we acquired *z*-stacks of images in RTF-

296    cleared mouse embryos. Comparing the achievable imaging depths with the OASIS micro-

297    scope in non-cleared (30 µm, **Fig. 3***A and* **S5***A*) *vs.* RTF-cleared samples (90 µm, **Fig. 3***B* and

298    **S5***A*) we noted the 3-fold larger attainable imaging depth and well-preserved structural details.

299    Next, we evaluated the photobleaching with the OASIS and confocal microscope. We first

300    compared 2P-light sheet and confocal acquisition at shallow imaging depths, by continuously

301    recording images of the same region of interest (ROI) at 30-µm depth in an non-cleared

302    embryo. At the same initial signal-to-noise ratio for both microscopes, We observed a ~3%-

303    intensity loss after the first image with the OASIS microscope ($t_{\exp}$ = 480 ms per image, 15.7

304    mW/spot for the OASIS), whereas the signal remained relatively stable after a confocal scan.

305    Fitting a monoexponential with the OASIS bleaching data revealed a 1/e (37%) loss of

306    fluorescence every 21 frames, **Fig. 3***C*. Thus, fs-pulsed non-linear excitation results in a

307    significantly higher pleaching in superficial tissue layers. However, for 3-D imaging of

308    thicker sections, confocal microscopy rapidly produced much faster photobleaching than the

309    OASIS because it required higher and higher laser powers to maintain image contrast at

310    greater imaging depths; in fact, acquiring the first complete *z*-stack with the CSLM attenuated

311    the TO-PRO-3 fluorescence so much that a second acquisition was impossible, **Fig. 3***D*.

312    We attribute the much higher volume photobleaching upon 1P confocal imaging in

313    non-cleared embryos to four reasons, (*i*), tissue scattering at 633 nm was roughly double that

314    of near-infrared light. The exponential scattering losses of excitation photons must be

315    compensated for by exponentially increasing the excitation powers with increasing imaging

316    depth; (*ii*), as a consequence of linear (1P) excitation, off-focus excitation of fluorophores

317    located above and below the imaged plane causes bleaching, too, i.e., at any plane, bleaching

318    occurs throughout the entire tissue volume while only one plane is imaged; (*iii*), although not

319    contributing to imaging, the scattered 1P excitation light neverthelass excites (out-of-focus)

320    fluorescence, which – in addition to the ballistic out-of-focus excitation – additionally

321    contributes to photobleaching. Non-linear (2P) excitation, on the other hand, confines both

322    fluorescence excitation and photobleaching to the focal plane, with the result fo better

323    preserving the sample outside the plane which is actually imaged; (*iv*), image acquisition was

324    4-times faster on the OASIS compared to confocal scans (480 ms/image *vs.* 1.815 s/image for

325    a similar image contrast), reducing the overall exposure of the sample.

326    We note that he better performance of the OASIS concept comes essentially from the

327    excitation side, because with a confocal pinhole of 2 Airy, on the fluorescence collection side,

328    both instruments should perform similarly. Finally, not only taking into account the loss of

329    signal, but also that of Weber contrast, we found a three-fold larger effective depth pene-

330    tration for the OASIS microcope, **Fig. S5***A*.

331    Taken together, the OASIS microscope combines the advantages of 2P-exciation and

332    wide-field imaging. Compared to the 1P-confocal, it achieves higher *z*-resolution, affords less

333    photobleaching in 3-D samples and considerably speeds up data acquisition, thus allowing a

334    more efficient and less invasive volume imaging.

335    (figure 3 close to here)

336

337

338    **Fast volume acquisition from mouse embryonic bodies and brain organoids**

339    We continued our comparison by imaging day-7 embryonic bodies (EB), **Fig. 4***A*, again

340    stained with TO-PRO3. Images acquired at different depths displayed rounded structures with

341    *lumina* inside tissue and revealed strong mitotic activity, **Fig. 4***B*. The rounded structures

342    presumably correspond to neuroepithelial-like structures that are readily formed within EBs,

343    indicating the inherent ability of the ectoderm to differentiate into neural lineages [42]. The

344    sub-µm resolution of the OASIS microscope allowed us the detailed characterization of the

345    different mitotic figures throughout the entire 160-µm thickness of the EB, **Fig. 4***C*.

346         Acquirig a 3-D image stack at a *z*-spacing of 0.5 µm (**Fig. S5***B*) allowed us

347    reconstructing complete EBs and realizing high-resolution projections along the orthogonal

348    axes, **Fig. 4***D*, revealing fine structural detail and including again mitosis across its entire

349    volume, **Fig. 4***E*. Volume imaging of entire EBs was almost 4-times faster with the OASIS

350    compared to the CLSM (a 200-µm *z*-stack with a 0.5µm z-spacing required 3'12" vs. 12'6"),

351    with no detectable photobleaching. Together, these features make the OASIS microscope an

352    ideal setup for 3-D the detailed characterization of EB development.

353    (figure 4 close to here)

354

355    Similar if not larger *z*-stacks were acquired a from RTF-cleared day-11 brain organoids, **Fig.**

356    **5***A*. At this early developmental stage, the neuroepithelium has been induced and forms buds

357    that undergo 3-D growth within the Matrigel droplets [43]. Our observations highlight strong

358    morphological modifications during this tissue expansion. A recurrent feature was that TO-

359  PRO-3 labeled nuclei were rounded just below the surface of the brain organoids, whereas

360  polymorph and diamond-shapes prevailed at greater imaging depths, **Fig. 5***B*. Also, the cell

361  density and nuclear labeling changed markedly with depth. Orthogonal planes revealed

362  compact groups of nuclei with stronger fluorescence, **Fig. 5***C*, as well as cavities and rounded

363  structures with a neuroepithelium-like shape. As before in EBs, the resolution of the OASIS

364  microscope allowed us to detect the presence of mitotic figures at the luminal side, **Fig. 5***D*. In

365  brain organoids, typical achievable imaging depths were around 200 μm, reflecting the

366  densification and opacification of the tissue during the development of an EB towards a brain

367  organoid.

368      With its large field-of-view, increased depth penetration, low photobleaching and

369  greater speed of acquisition compared to the CSLM, the OASIS optical scheme lends itself

370  ideally to the observation of entire EBs and whole brain organoids. Thin sections can be

371  studied at depth with sub-cellular (μm-) resolution, without mechanical slicing. The reduced

372  complexity compared to a classical light-sheet microscope, its compact mono-block design

373  and comparble ease-of-use make it an ideal companion for functional neuroanatomy. The

374  ongoing integration of a compact, fixed-wavelength high-power fs-pulsed laser into this

375  package will make the OASIS a unique, portable, alignment-free bench-top 2P-microcope.

376
377  (figure 5 close to here)
378
379
380
381  **CONCLUSION**
382
383  Work on brain organoids offers several distinctive advantages over classical disease models:

384  (*i*), derived from patient fibroblasts, they raise less concerns than animal experimentation and

385  work on human explants (see, however, [44] for an emerging awareness of the ethical issues

386  associated with these 3-D cultures); (*ii*), they avoid the limitations of animal models that are

387  often only a poor proxy of human pathology; (*iii*), they allow studies of rare or sporadic cases,

388    for which genetic models are missing; (*iv*), they allow observing the onset of the disease

389    during the early steps of the brain development, opening opportunities for studies that would

390    be impractical or inacceptable on human embryos or infants.

391       For this field of applications, the OASIS 2P virtual light-sheet microscope is a

392    compact, versatile and cost-efficient 2P wide-field research instrument allowing imaging of

393    hiPSC cultures, embryonic bodies and brain organoids.

394
395
396
397
398
399
400    **MATERIALS AND METHODS**
401
402
403    **Ethics statement**
404
405    All experimental procedures were performed in accordance with the French legislation and in
406    compliance with the European Community Council Directive of November 24, 1986
407    (86/609/EEC) for the care and use of laboratory animals. The used protocols were approved
408    by the local ethics committee.
409
410
411    **Sample preparation**
412
413    *hiPSC culture and formation of embryonic bodies.* Episomal human induced pluripotent stem
414    cells (hIPSCs, Gibco) were cultivated on mitomycin-treated mouse embryonic fibroblasts
415    using DMEM/F12 medium (Invitrogen), supplemented with 10% knockout serum (Gibco).
416    When hIPSCs had reached about 80% confluence, they were detached with versene
417    (ThermoFisher). Cell aggregates were removed and a single-cell suspension obtained with a
418    cell strainer having a 100-μm mesh size (Corning). For the formation of embryoid bodies
419    (EBs), $10^4$ cells were inoculated in 100 μl in each well of a ultra-low attachment, round-
420    bottomed 96-well plate (Corning) and cultivated during 9 days in EB formation medium
421    (StemCell Technologies).
422
423    *Mouse embryos.* Embryos were age E10.5 and E14.5. Mice were killed by cervical
424    dislocation, the abdominal cavity was opened and the uterine horns were removed. Embryos
425    were collected under a macroscope (Nikon SMZ800) and immersed in formalin (buffered
426    10% formaldehyde, VWR) overnight. They then were stored at 4°C in PBS / Sodium Azide
427    0,02%. E10.5 embryos were used for whole-embryo transparisation; E14.5 embryos were
428    embedded in Optimal Cutting Temperature (OCT) compound and sliced into 7-μm-thin
429    sections on a cryotome (Cryocut 1800, Leica).
430
431

432 **Staining, clearing and embedding**

433

434 *Nuclear staining*. Samples were permeabilized by a 0.2% TritonX100 solution in PBS (during
435 15 min for 7-µm-thin embryo slices and EBs, 20 min for brain organoids, 1h for the whole-
436 mount E10.5 embryo). They were then incubated overnight in a 1:1000 solution of TO-PRO3
437 (Invitrogen) or of chloroform-purified Methyl Green (Merck) in PBS and finally washed in
438 PBS. At this point, non-cleared samples were mounted in a PBS-filled chamber under a glass
439 coverslip for microscopy. We used a home-made recording chamber, that was modified from
440 chambers designed for imaging and available as 3-D printer templates:
441 https://idisco.info/idisco-protocol/).

442

443 *Clearing*. After nuclear staining, samples were processed for one of the three following
444 clearing methods: TDE [39], Clear[T2] [40] or RTF [41].

445

446 *TDE*. Samples were successively immersed in increasing concentrations (20%, 40% and 60%)
447 of TDE (Sigma) solutions in PBS. The duration of each incubation varied as a function of the
448 sample size: 1 h for 7-µm embryo slices and for EBs, 3 h for a whole E10.5 embryo.

449

450 *Clear[T2]*. Samples were immersed successively in, (*i*), a 25% formamide (Sigma) / 10%
451 polyethylene glycol (PEG8000, Merck) solution in PBS (10 min for embryo slices and
452 embryonic bodies, 30 min for a whole E10.5 embryo); (*ii*), a 50% formamide / 20% PEG8000
453 solution in PBS (5 min for slices and EBs, 15 min for whole embryo); (*iii*), a 50% formamide
454 / 20% PEG8000 solution in PBS (1h for slices and for EBs, 3h for a whole E10.5 embryo).

455

456 *RTF*. Samples were successively immersed in, (*i*) a 30% triethanolamine (TEA, Sigma) / 40%
457 formamide (Sigma) solution (15 min for slices and for embryonic bodies, 20 min for brain
458 organoids, 3h20min for a whole E10.5 embryo); (*ii*) a 60% TEA / 25% formamide solution
459 (25 min for slices and for embryonic bodies, 30 min for brain organoids, 5 h for embryo); (*iii*)
460 a 70% TEA / 15% formamide solution (25 min for slices and for EBs, 30 min for brain
461 organoids, 5 h for whole embryo). In either case, after clearing, samples were mounted under
462 a glass coverslip in a chamber filled with the respective final solution.

463

464

465 **Microscopy**

466

467 *Confocal microscopy.* We used a Zeiss LSM 710 microscope with a ×63/1.4NA oil-
468 immersion objective, for the acquisition of the confocal data shown in figs. 2 and S3, and a
469 ×40/1.0NA water-immersion objective for tissue sections and thick samples (embryo, EB,
470 brain organoid), respectively. For a fair comparison of the performance for imaging thick
471 samples of the confocal and 2P-virtual light sheet OASIS microscope, we set the confocal
472 pinhole to 2 Airy units and the scanned area was restricted to $900 \times 900$ pixels with a zoom
473 resulting in an effective pixel size of 0.182 µm, equivalent to the OASIS. We also acquired
474 confocal images at 1 Airy for comparison. The laser powers delivered to the sample are
475 indicated in each figure. For 1PEF, we excited TO-PRO3 using the 633-nm line of a HeNe
476 gas laser (Lasos). Fluorescence was collected in between 646 nm and 725 nm.

477

478 *2P-virtual light-sheet microscopy*. The optical path of OASIS microscope is schematized in
479 Fig.1. A detailed technical characterization is given in a companion paper, (Ricard, Deeg, *et*
480 *al., submitted)*. Briefly, 2P fluorescence is excited in 40 foci. These spots are scanned across
481 the sample and the fluorescence emission from the spots confocally detected, similar to a

482   Nipkow-Petráň spinning-disk microscope [45]. However, for optimal 2P excitation, a disk
483   was manufactured that combines micro-lenses, dielectric long-pass (LP) coating and confocal
484   pinholes. On the front side of this glass disk (borofloat B33, 100-mm diameter, 2-mm thick)
485   >5,000 micro-lenses are arranged in four nested spirals were micro-machined (diameter $D$ =
486   666 µm, focal length $f$ = 7.8mm, lens-area-fill factor: 73.2%, the average inter-lens spacing is
487   about 666 µm). The dielectric coating ($T_{ave}$ < 0.05% for 400-675 nm, $T_{ave}$ > 93% for 730-1100
488   nm) on the rear side has pinholes (i.e. non-coted areas, each having 60-µm diameter) centered
489   on the micro-lenses on the front side of the disk (see Fig.1, *inset*).
490
491   For 2P excitation, the Gaussian beam of a fs-pulsed Ti:Saph laser (Spectra-Physics
492   MaiTai HP with DeepSee$^{TM}$ module) was shuttered (AOM: AA Opoelectronic), expanded and
493   collimated to a beam diameter of about 5 mm ($1/e^2$) and aligned on the rear side of the disk.
494   The disk transmits the IR light and the microlenses on the front side generate a spiral pattern
495   of foci 7.8 mm in front of the disk. This pattern is imaged onto the sample by a telescope
496   formed by the tube lens ($f$ = 200 mm) and water-immersion objective (Nikon CFI75
497   Apochromat LWD 25× MP, NA 1.1w).
498
499   2PEF is detected through the same objective and tube lens. However, between the tube
500   lens and the disk, two LP dichroics (custom design and manufacture from Alluxa, 50%-cut-on
501   at 705 nm, $T_{ave}$ < 1.5% from 400-695 nm, $T_{ave}$ > 96% from 715 - 1100nm, flatness < 0.25
502   wave P-V per inch, $d$ = 1mm) were used at 18° angle of incidence (AOI) to image the
503   emission from the excitation spots onto the pinholes of the disk. As a consequence, the
504   collected fluorescence from the excitation spots arrives focused at the level of the pinholes
505   whereas out-of-focus fluorescence and scattered emission light is blocked. The intermediate
506   image in the pinhole plane is separated from the IR excitation light by an AOI 45° primary
507   dichroic LP filter (Custom design, manufactured by Alluxa, AOI 45°, flatness < 0.25 wave P-
508   V per inch, $d$ = 1 mm) and magnified by a $f_1$ = 140 mm and $f_2$ = 200 mm telescope onto an
509   sCMOS camera (PCO.edge 4.2, chip size 13.3 mm x 13.3 mm). Due to this magnification, the
510   image size on the chip is about 7.1 mm and the total magnification of the system is ×36. To
511   block residual IR excitation light, a multi-photon-emitter (ET700SP-2P, Chroma) was used.
512   For dual-color imaging a LP dichroic under AOI 15° (in fact a Semrock 532-nm laser
513   BrightLine Di02-R532, AOI = 45°. For AOI = 15° its edge shifts to 568 nm) was used in
514   combination with a knife-edge right-angle prism to split the image in the non-infinity space
515   between the $f$ = 200-mm lens and the camera chip. The red emission (>568nm) is imaged on
516   one half of the sCMOS chip, and the green (<568nm) on the other, without further emission
517   filtering. The fluorescence signal at the margin of the field of view is relatively weak, and
518   cropping the image of about 7.1-mm diameter to the half chip size of 6.65 mm x 13.3 mm is
519   justified. Image cropping, rotation and alignment were automatized in a custom-written macro
520   in FIJI [46].
521
522   The upright microscope body was constructed as a rugged monocoque, machined from
523   a single metal block (see photos), with slots for the optical and opto-mechanical elements at
524   pre-defined places. A highly folded realization of the beam-path optimized by ZEMAX
525   allowed the compact design. We used a voice-coil based *z*-objective drive, combining accu-
526   racy and precision over a wide focusing range. A flipable mirror was used to toggle between
527   2P-imaging and trans- or reflected-light imaging. This alternative beam path uses a different $f$
528   = 140-mm tube lens in combination with a small USB camera (Point Grey, BFLY-U3-
529   23S6M-C). Having an effective magnification of ×17.5 this imaging mode was used for
530   getting an overview of the sample and for identifying regions of interest (ROIs) to be imaged
531   in 2P fluorescence. All image acquisition parameters, the laser and the objective focus drive

532 were controlled through an in-house microcontroller imaging software. The used excitation
533 wavelength $\lambda_{ex}$, laser power $<P>$, and z-spacing $\Delta z$ for stacks were software controlled and
534 are specified in the figure legends. Images were acquired without software binning at the full
535 sCMOS resolution.
536
537
538
539 **Image analysis and quantification**
540
541 Images were analyzed and displayed using FIJI. For a better visibility of the faint fluorescent
542 signals at greater imaging depths, we used a nonlinear look-up table ($\gamma = 0.6$) for Figs. 4B-E
543 and 5C-D.
544
545 Weber contrast was calculated as $C_w = (F-B)/B$, where $F$ and $B$ are the fluorescence intensities
546 of the image and background, respectively. $B$ was measured as the mean intensity of a cell-
547 free region and $F$ corresponded to the mean intensity in a small ROI (18 µm x 18µm) in the
548 center of the image for fig. S5A, and to the whole image in fig. S5B. (In fig. S5A the sample
549 was inclined respect to the optical axis so that only a small region could be used to quantify
550 the penetration depth).
551
552
553
554 **Statistics**
555
556 Results are at least triplicates of three experiments and are represented as mean ± SD.
557 Student's *t*-test was used to compare among experiments. Data were processed and figures
558 prepared using IGOR Pro (Wavemetrics).
559

560 **List of abbreviations**
561
562 2P          -          two-photon
563
564 3-D          -          three-dimensional
565
566 AOI          -          angle of incidence
567
568 BSA          -          bovine serum albumin
569
570 CLSM          -          confocal laser scanning microscope
571
572 DMEM          -          Dulbecco's modified Eagle medium
573
574 EB          -          embryonic body
575
576 FWHM          -          full-width at half maximum
577
578 hiPSC          -          human inducible pluripotent stem cell
579
580 LP          -          long-pass (filter)
581 MG          -          Magnesium Green
582
583 NA          -          numerical aperture
584
585 OASIS          -          On-axis 2-photon light-sheet generation *in-vivo* imaging system
586
587 OCT          -          opimal cutting temperature
588
589 PBS          -          phosphate-buffered solution
590
591 PEG          -          polyethylene glycol
592
593 RI          -          refractive index
594
595 ROI          -          region of interest
596
597 RTF          -          Rapid clearing method based on Triethanolamine and Formamide
598
599 sCMOS          -          scientific Complementary Metal Oxide Semiconductor
600
601 SD          -          standard deviation
602
603 SPIM          -          selective-plane illumination
604
605 TDE          -          2,2'-thiodiethanol
606
607 TO-PRO-3      -          a carbocyanine monomer nucleic acid stain with red excitation and far-
608                                     red fluorescence (642 nm/661 nm) similar to Alexa Fluor 647 or Cy5. It
609                                     is among the highest-sensitivity probes for nucleic acid detection.

**Author contributions**

AD and RU designed and conceptualized the OASIS prototype, BD and PD generated iPSCs, embryonic bodies and brain organoids, AD, BD, IR, CR, MB and MO performed experiments, MO wrote the paper with contributions from all authors.

**REFERENCES**

[1] Rakotoson, I. *Validation d'une approche de microscopie optique pour l'étude morpho-fonctionnelle des corps embryoïdes et mini-brains issus d'hIPSC*, Faculté des Sciences Fondamentales et Biomédicales, Master of Science, Université Paris Descartes, (2018), 33 pages.

[2] Gonzalez, D., Gregory, J., and Brennand, K.J. (2017) The Importance of Non-Neuronal Cell Types in hiPSC-Based Disease Modeling & Drug Screening. *Front. Cell Dev. Biol.* 5: 117.

[3] Fatehullah, A., Tan, S.H., and Barker, N. (2016) Organoids as an in vitro model of human development and disease. *Nat. Cell Biol.* 18: 246.

[4] Giandomenico, S.L., and Lancaster, M.A. (2017) Probing human brain evolution and development in organoids. Curr. Op. *Cell Biol.* 44: 36-43.

[5] Lancaster, M.A., Renner, M., Martin, C.-A., Wenzel, D., Bicknell, L.S., Hurles, M.E., Homfray, T., Penninger, J.M., Jackson, A.P., and Knoblich, J.A. (2013) Cerebral organoids model human brain development and microcephaly. *Nature* 501  373.

652  [6] Kelava, I., and Lancaster, M.A. (2016) Dishing out mini-brains: current progress and
653        future prospects in brain organoid research. *Dev. Biol.* 420: 199-209.

654  [7] Mansour, A.A., Gonçalves, J.T., Bloyd, C.W., Li, H., Fernandes, S., Quang, D., Johnston,
655        S., Parylak, S.L., Jin, X., and Gage, F.H. (2018) An *in vivo* model of functional and
656        vascularized human brain organoids. *Nat. Biotech.* 36: 432.

657  [8] Wan, P., Zhu, J., Xu, J., Li, Y., Yu, T., and Zhu, D. (2018)  Evaluation of seven optical
658        clearing methods in mouse brain. *Neurophotonics* 5: 035007.

659  [9] Renner, M., Lancaster, M.A., Bian, S., Choi, H., Ku, T., Peer, A., Chung K., and
660        Knoblich, J.A. (2017) Self-organized developmental patterning and differentiation in
661        cerebral organoids. *EMBO J.* e201694700.

662  [10] Hama, H., Hioki, H., Namiki, K., Hoshida, T., Kurokawa, H., Ishidate, F., Kaneko, T.,
663        Akagi, T., Saito, T., and Saido, T. (2015) ScaleS: an optical clearing palette for
664        biological imaging. *Nat. Neurosci.* 18:  1518.

665  [11] Huisken, J., Swoger, J., Del Bene, F., Wittbrodt, J., and Stelzer, E.H.K. (2004) Optical
666        sectioning deep inside live embryos by selective plane illumination microscopy.
667        *Science* 305: 1007-1009.

668  [12] Keller, P.J., Schmidt, A.D., Wittbrodt, J., and Stelzer, E.H.K. (2008) Reconstruction of
669        zebrafish early embryonic development by scanned light sheet microscopy. *Science*
670        322: 1065-1069.

671  [13] Santi, P.A. (2011) Light sheet fluorescence microscopy: a review. *J. Histochem.*
672        *Cytochem.* 59: 129-138.

673  [14] Stelzer, E.H.K. (2015) Light-sheet fluorescence microscopy for quantitative biology.
674        *Nat. Methods* 12: 23-26.

675  [15] Truong, T.V., Supatto, W., Koos, D.S., Choi, J.M., and Fraser, S.E. (2011) Deep and fast
676        live imaging with two-photon scanned light-sheet microscopy. *Nat. Methods* 8: 757.

677  [16] Mahou, P., Vermot, J., Beaurepaire, E., and Supatto, W. (2014) Multicolor two-photon
678        light-sheet microscopy. *Nat. Methods* 11: 600.

679  [17] Baumgart, E., and Kubitscheck, U. (2012) Scanned light sheet microscopy with confocal
680        slit detection. *Opt. Express* 20: 21805-21814.

681  [18] Vettenburg, T., Dalgarno, H.I., Nylk, J., Coll-Lladó, C., Ferrier, D.E., Čižmár, T., Gunn-
682        Moore, F.J., and Dholakia, K. (2014) Light-sheet microscopy using an Airy beam.
683        *Nat. Methods* 11: 541.

684  [19] Fahrbach, F.O., Gurchenkov, V., Alessandri, K., Nassoy, P., and Rohrbach, A. (2013)
685       Light-sheet microscopy in thick media using scanned Bessel beams and two-photon
686       fluorescence excitation. *Opt. Express* 21: 13824-13839.

687  [20] Zhao, M. Zhang, H., Li, Y,. Ashok, A., Liang, R., Zhou, W., and Peng, L. (2014)
688       Cellular imaging of deep organ using two-photon Bessel light-sheet nonlinear
689       structured illumination microscopy. *Biomed. Opt. Express* 5: 1296-1308.

690  [21] Müllenbroich, M.C., Turrini, L., Silvestri, L., Alterini, T., Gheisari, A., Vanzi, F.,
691       Sacconi, L., and Pavone, F.S. (2018) Bessel beam illumination reduces random and
692       systematic errors in quantitative functional studies using light-sheet microscopy.
693       *Front. Cell. Neurosci.* 12: 315.

694  [22] Andilla, J., Jorand, R., Olarte, O.E., Dufour, A.C., Cazales, M., Montagner, Y.L.,
695       Ceolato, R., Riviere, N., Olivo-Marin, J.-C., and Loza-Alvarez, P. (2017)  Imaging
696       tissue-mimic with light sheet microscopy: A comparative guideline. *Sci. Rep.* 7:
697       44939.

698  [23] Elisa, Z., Toon, B., De Smedt, S.C., Katrien, R., Kristiaan, N., and Kevin, B. (2018)
699       Technical implementations of light sheet microscopy. *Microsc. Res. Tech.* <u>early view</u>
700       https://doi.org/10.1002/jemt.22981.

701  [24] Holekamp, T.F., Turaga, D., and Holy, T.E. (2008) Fast three-dimensional fluorescence
702       imaging of activity in neural populations by objective-coupled planar illumination
703       microscopy. *Neuron* 57: 661-672.

704  [25] McGorty, R., Liu, H., Kamiyama, D., Dong, Z., Guo, S., and Huang, B. (2015) Open-top
705       selective plane illumination microscope for conventionally mounted specimens. *Opt.*
706       *Express* 23: 16142-16153.

707  [26] Chen, B.-C., Legant, W.R., Wang, K., Shao, L., Milkie, D.E., Davidson, M.W.,
708       Janetopoulos, C., Wu, X.S., Hammer, J.A., and Liu, Z. (2014) Lattice light-sheet
709       microscopy: imaging molecules to embryos at high spatiotemporal resolution. *Science*
710       346: 1257998.

711  [27] Reynaud, E.G., Peychl, J., Huisken, J., and Tomancak, P. (2014) Guide to light-sheet
712       microscopy for adventurous biologists. *Nat. Methods* 12: 30.

713  [28] Oheim, M., Beaurepaire, E. Chaigneau, E., Mertz, J., and Charpak, S. (2001) Two-
714       photon microscopy in brain tissue: parameters influencing the imaging depth. *J.*
715       *Neurosci. Meth.* 111: 29-37.

716  [29] Bewersdorf, J., Pick, R., and Hell, S.W. (1998) Multifocal multiphoton microscopy. *Opt.*
717       *Lett.* 23: 655-657.

718     [30] Egner, A., Andresen, V., and Hell, S.W. (2002) Comparison of the axial resolution of
719             practical Nipkow‑disk confocal fluorescence microscopy with that of multifocal
720             multiphoton microscopy: Theory and experiment. *J. Microsc.* 206: 24-32.

721     [31] Shimozawa, K.Y., Kondo, T., Hayashi, S., Shitamukai, A., Konno, D., Matsuzaki, F.,
722             Takayama, J., Onami, S., Nakayama, H., and Kosugi, Y. (2013) Improving spinning
723             disk confocal microscopy by preventing pinhole cross-talk for intravital imaging.
724             *Proc. Natl. Acad. Sci. USA* 110: 6241.

725     [32] König, K., Multiphoton Microscopy and Fluorescence Lifetime Imaging: Applications in
726             Biology and Medicine, Walter de Gruyter GmbH & Co KG, 2018.

727     [33] Bink, K., Walch, A., Feuchtinger, A., Eisenmann, H., Hutzler, P., Höfler, H., and
728             Werner, M. (2001) TO-PRO-3 is an optimal fluorescent dye for nuclear
729             counterstaining in dual-colour FISH on paraffin sections. *Histochem. Cell. Biol.* 115:
730             293-299.

731     [34] Prieto, D., Aparicio, G., Morande, P.E., and Zolessi, F.R. (2014) A fast, low cost, and
732             highly efficient fluorescent DNA labeling method using methyl green. *Histochem Cell
733             Biol.* 142: 335-345.

734     [35] Smith, P.G., Baldacchini, T., Carter, J., and Zadoyan, R. (2012) Two-photon micro-
735             scopy/mutlimodal imaging: Femtosecond laser developments advance two-photon
736             imaging. BioOptics World 5. http://www.biopticsworld.com/articles/print/volume-
737             5/issue-04/features/femtosecond-laser-developments-advance-two-photon-
738             imaging.html.

739     [36] Ricard, C., Arroyo, E.D., He, C. X., Portera-Cailliau, C., Lepousez, G., Canepari, M.,
740             and Fiole, D. (2018) Two-photon probes for *in vivo* multicolor microscopy of the
741             structure and signals of brain cells. *Brain Structure and Function* 223: 3011–3043.

742     [37] Schmidt, E.M., and Oheim, M. (2018) Two-photon imaging induces brain heating and
743             calcium microdomain hyper-activity in cortical astrocytes. *bioRxiv* 321091.

744     [38] Richardson, D.S., and Lichtman, J.W. Clarifying tissue clearing. *Cell* 162: 246-257.

745     [39] Aoyagi, Y., Kawakami, R., Osanai, H., Hibi, T., and Nemoto, T. (2015) A rapid optical
746             clearing protocol using 2, 2-thiodiethanol for microscopic observation of fixed mouse
747             brain. *PloS One* 10: e0116280.

748     [40] Kuwajima, T., Sitko, A. A., Bhansali, P., Jurgens, C., Guido, W., and Mason, C. (2013)
749             Clear^T: a detergent-and solvent-free clearing method for neuronal and non-neuronal
750             tissue. *Development* 140: 1364-1368.

751   [41] Yu, T., Zhu, J., Li, Y., Ma, Y., Wang, J., Cheng, X., Jin, S., Sun, Q., Li, X., and Gong,
752        H. (2018) RTF: a rapid and versatile tissue optical clearing method. *Sci. Rep.* 8: 1964.

753   [42] Ying, Q.-L., and Smith, A.G. (2003) Defined conditions for neural commitment and
754        differentiation. *Meth. Enzymol.* 365: 327-341.

755   [43] Lancaster, M.A., and Knoblich, J.A. (2014) Generation of cerebral organoids from
756        human pluripotent stem cells. *Nat. Protoc.* 9: 2329.

757   [44] Farahany, N., Greely, H., Hyman, S., Koch, C., Grady, C., Pa□ca, S., Sestan, N., Arlotta,
758        P., Bernat, J., and Ting, J. (2018) The ethics of experimenting with human brain
759        tissue. *Nature* 556: 429.

760   [45] Kino, G.S. Intermediate optics in Nipkow disk microscopes. *in*: Pawley, J.B. (Ed.),
761        Handbook of Biological Confocal Microscopy, 1995, pp. 155-165.

762   [46] Schindelin, J., Arganda-Carreras, I., Frise, E., Kaynig, V., Longair, M., Pietzsch, T.,
763        Preibisch, S., Rueden, C., Saalfeld, S., and Schmid, B. (2012) Fiji: an open-source
764        platform for biological-image analysis. *Nat. Methods* 9: 676.

765

766

## FIGURE LEGENDS

768
769

770   **Fig.1** *Layout and performance of the OASIS two-photon microscope*. **A.** Simplified optical
771   path of the custom 2P virtual light-sheet microscope. *Red*: IR excitation, *green*: fluorescence.
772   Ti:Sapph – fs-pulsed IR laser; DS – DeepSee; BE – beam expander; $\pi$-shaper – optical ele-
773   ment that converts the Gaussian beam into a top hat profile; M – mirrors; dic – dichroic mir-
774   rors; SD – spinning disk; TL – tube lens; CDE – corrective distance element; OL – objective
775   lens; ISD – image-splitting device; sCMOS – camera. *Inset* ❶: generated multi-spot
776   excitation pattern und epi-collection of the generated fluorescence through the same objective.
777   *Inset* ❷: detail of microlens/pinhole/dichroic coating arrangement. Note the offset between
778   the excitation (exc.) and fluorescence foci (fluo.) at the level of the disk, produced by the
779   CDE. **B.** Depth penetration in turbid samples. Log-plot of 2P-excited fluorescence from a
780   green-fluorescent Chroma test slide, topped either with water (0%) or increasing
781   concentrations of milk (a model for the multi-scale scatterers present in tissue), for the OASIS
782   (red dots) and a ZEISS LSM710. Confocal pinhole diameters were 1 and 2 Airy, as indicated.
783   **C.** OASIS prototype, note the compact size and space available around the objective, *inset*.
784   VCD – voice coil $z$ drive; BFC – bright-field camera. **D.** OASIS lateral resolution. Equatorial
785   section through an autofluorescent thorny pollen grain. Scale bar, 10 µm. *Inset*: magnified

786   view of an individual spine and intensity profiles across the lines shown; Scale bar, 2 µm. **E.**

787   OASIS *z-* resolution. Axial-intensity profile measured from a *z*-stack of images acquired from

788   a green fluorescent Chroma slide (solid line), and its derivative *dF/dz* (dashed). The FWHM,

789   equiva-lent to the 10-90% intensity range, was taken as axial optical sectioning capacity *Δz*.

790   **Fig. 2** *Comparison of the used nuclear stains and clearing methods.* **A.** *Left,* optical section of

791   a slice from an E14.5 embryo, labeled with TO-PRO3 or Methyl Green and observed on a

792   confocal laser scanning microscope (CLSM, *top*) or on the OASIS microscope (*bottom*).

793   Scale-bar, 10 µm. *Right,* relative fluorescence intensity of TO-PRO3 and Methyl Green in

794   nuclei of E14.5 embryo slices measured on a CLSM (*top right*) or on the OASIS (*bottom*

795   *right*). **B.** TO-PRO3 (*top*) and Methyl Green (*bottom*) 2P-excitation spectra. Color code as in

796   (A). **C.** Macrophotographies of E10.5 embryos in control (PBS) and following three clearing

797   protocols (Clear$^{T2}$, RTF and TDE 60%). Note the variable degree of transparisation and the

798   volume change. **D.** Relative fluorescence of TO-PRO3-positiev nuclei in E14.5 embryo slices

799   observed on a CLSM after the same clearing protocols as above. Note the log-scale. * = *P <*

800   0.0001. **E.** Fluorescence loss upon clearing requires high laser powers. Confocal micrographs

801   of slices from an E14.5 embryo labeled with TO-PRO3 under control (*left*) and after RTF

802   clearing (*right*) along with the laser powers required to attain the same signal-to-background

803   ratio. Scale-bar, 10µm.

804

805   **Fig. 3** *The OASIS microscope outperforms a CLSM for 3-D embryo imaging.* **A.** 3-D data set

806   taken with the OASIS in a non-cleared embryo stained with TO-PRO3 (Control). Panels show

807   *xz-* projection of a *z*-stack of images (*right*) and *xy*-planes (*left*) corresponding to the dashed

808   lines at 30 µm (1) and 65 µm imaging depth (2), respectively. Scale-bar, 25 µm. **B.** same, at

809   32 µm (1) and 115 µm depth (2), respectively, for an RTF-cleared embryo. Scale-bar, 25 µm,

810   as in (A). **C.** Representative bleaching curves during continuous acquisitions, from a single *z*-

811   section in – respectively –a thin slice of intestine (*top*) and of TO-PRO3-labeled nuclei

812   (*bottom*) at 30-µm imaging depth in a embryo. **D.** Representative planes at various imaging

813   depths (15, 50 and 100 µm, respectively) of a 3-D data set (200 planes from the surface to 200

814   µm, *Δz* = 1µm;) acquired from a TO-PRO3-labled embryo. The 2 colums show the sections

815   during the 1$^{st}$ passage (*left*) and during the 2$^{nd}$ passage, after completion of the 1$^{st}$ image stack

816   (*right*). Note the almost complete bleaching prohibiting repetitive volume imaging for the

817   CSLM but not the OASIS microscope. Measured laser powers are given for each depth.

818   Scale-bar, 25 µm.

819

820 **Fig. 4** *3-D imaging with the OASIS of the fine structure of embryonic bodies (EBs).* **A.**
821 Macrophotography of a day-7 EB; Scale-bar, 300 µm. **B.** Image acquired in the center of the
822 organoid after TO-PRO3 staining, 50 µm below the surface. Scale-bar, 25 µm. Note the
823 presence of internal round structures with a lumen. **C.** Zoom on mitotic figures observed in
824 the EB at various depth (*top left*: prophase; *top right*: metaphase; *bottom left*: early anaphase;
825 *bottom right*: late anaphase); stain: TO-PRO3. Scale-bar for all panels, 10 µm. **D.** *xz*-pro-
826 jections of a *z*-stack acquired across an entire day-7, TO-PRO3-stained EB. Scale-bar, 25 µm.
827 Arrow points to mitosis also visible in panel (E). # indicates ventricle-like structure also
828 perceived in (E). **E.** *xy*-sections across the dotted lines shown in (D) at imaging depths of,
829 respectively, 42 µm (1), 75 µm (2) and 155 µm (3). Scale-bar, 25µm. With the exception of
830 (A), all images were acquired after RTF clearing.

831

832 **Figure 5.** *Brain organoid imaging with OASIS.* **A.** Macrophotography of a day 11 brain
833 organoid before clearing and observation on the OASIS microscope; scale-bar: 300 µm. **B.**
834 Image acquired in the center of the organoid at 45µm below the surface; stain: TO-PRO3;
835 scale-bar: 10µm. **C.** z-reconstruction (left) and xy-acquisition (right) at respectively 30µm (1),
836 80µm (2) and 125µm (3) below the surface of the organoid; stain: TO-PRO3; scale-bar:
837 25µm. Note the change of the morphology of the nuclei in the center of the region of interest
838 when depth increase. **D.** z-reconstruction (left) and xy-acquisition (right) at respectively 20µm
839 (1), 35µm (2) and 75µm (3) below the surface of the organoid; stain: TO-PRO3; scale-bar:
840 25µm. Note the globular structure (neuro-epithelium) that can also be observed on the
841 macroscopy and numerous mitosis inside this structure (arrows). Except in A. all images were
842 acquired after the clearing of the organoid with the RTF protocol. Note the image quality
843 across the entire imaged volume.
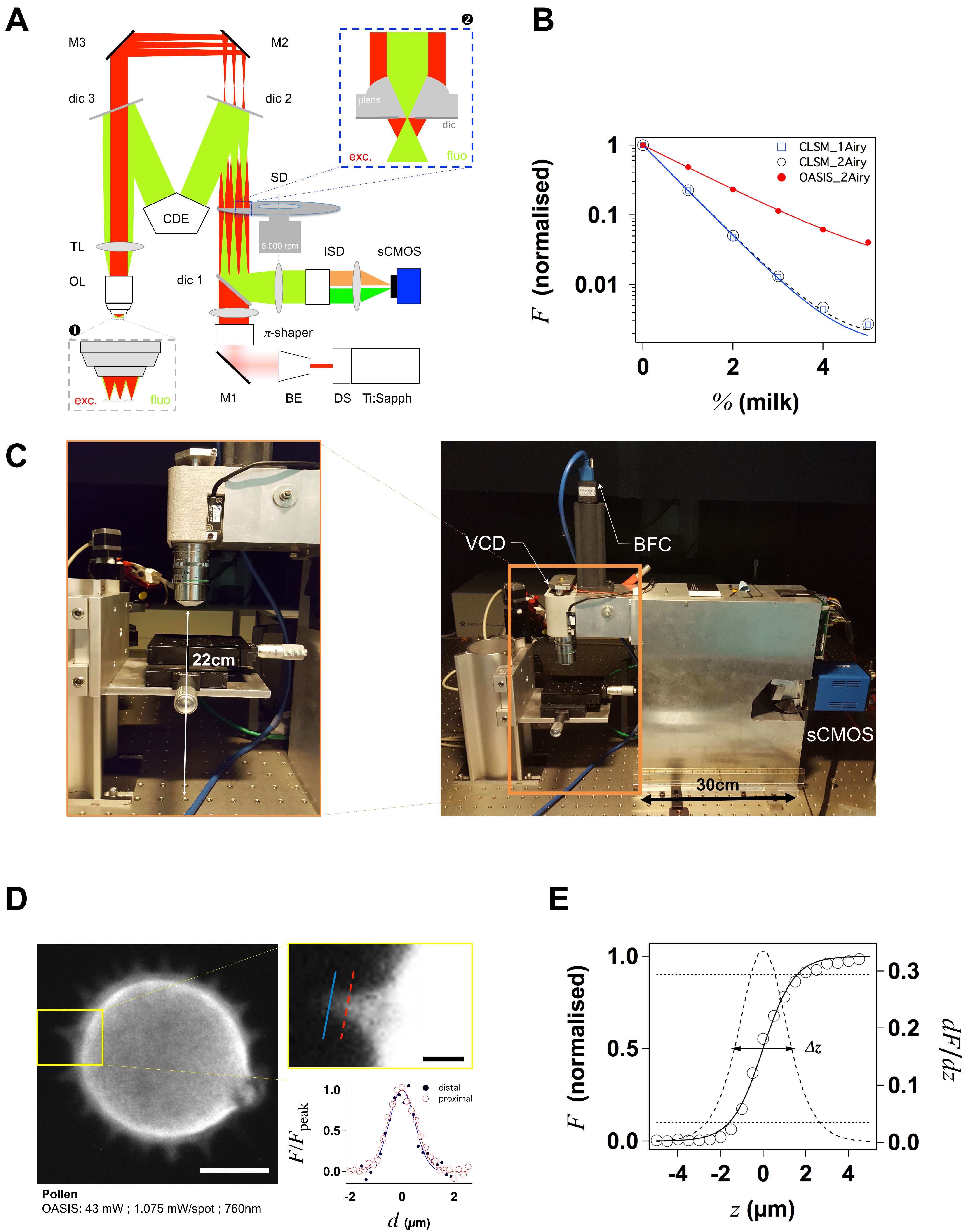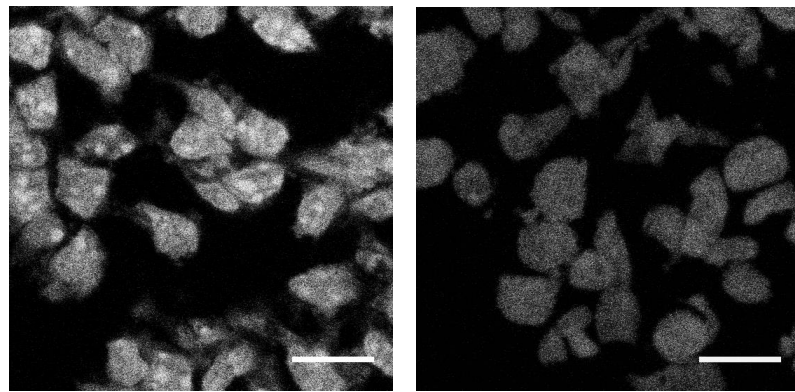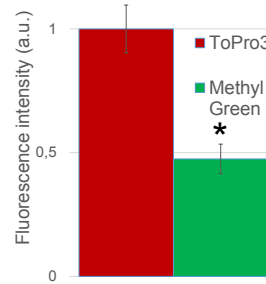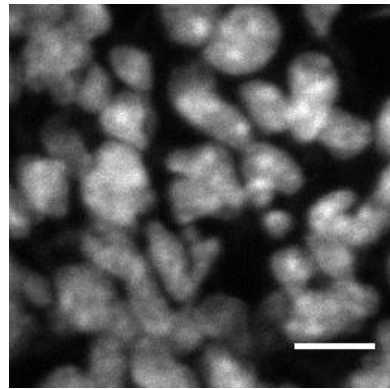
844
845
846
847

**A**

M3    M2

dic 3    dic 2

CDE

SD

2

μlens

dic

exc.    fluo

TL

OL

dic 1

ISD    sCMOS

5,000 rpm

1

exc.    fluo

π-shaper

M1    BE    DS    Ti:Sapph

**B**

CLSM_1Airy
CLSM_2Airy
OASIS_2Airy

$F$ (normalised)

$\%$ (milk)

**C**

22cm

VCD    BFC

sCMOS

30cm

**D**

Pollen
OASIS: 43 mW ; 1,075 mW/spot ; 760nm

distal
proximal

$F/F_{peak}$

$d$ (μm)

**E**

$F$ (normalised)

$\Delta z$

$dF/dz$

$z$ (μm)

**Figure 1**

# A



ToPro3
Confocal: 0,55 µW – 633nm

Methyl Green
Confocal: 0,55 µW – 633nm

ToPro3
OASIS: 309 mW ; 7,7 mW/spot ; 760nm
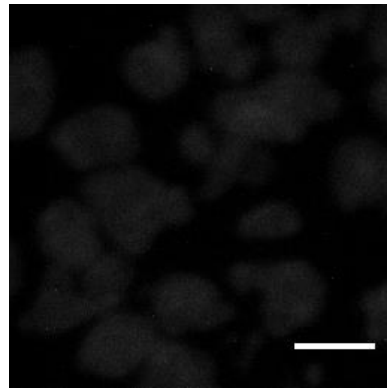
Methyl Green
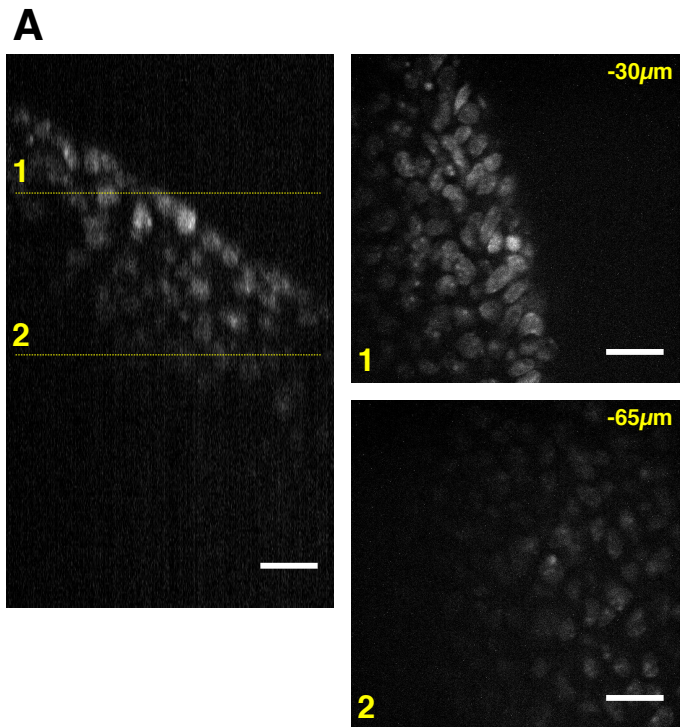OASIS: 309 mW ; 7,7 mW/spot ; 750nm

Fluorescence intensity
at 633nm

Fluorescence intensity
on the OASIS

# B

ToPro3 2hv
excitation spectrum

Methyl Green 2hv
excitation spectrum
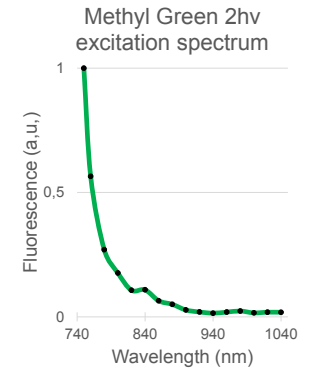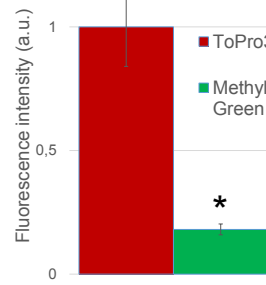
# C



Control

Clear T2

RTF

TDE 60%

# D

ToPro3 fluorescence under various clarification
methods (633nm @ 0,55µW)
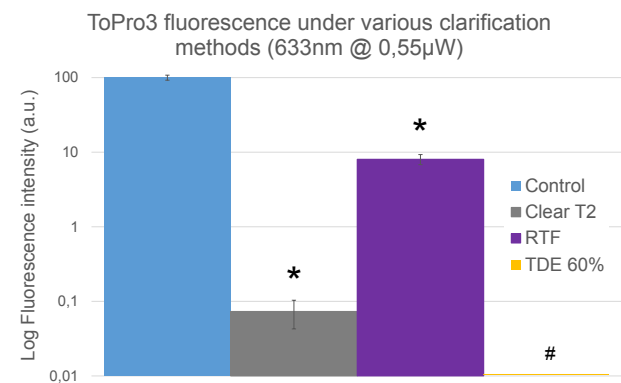
# E
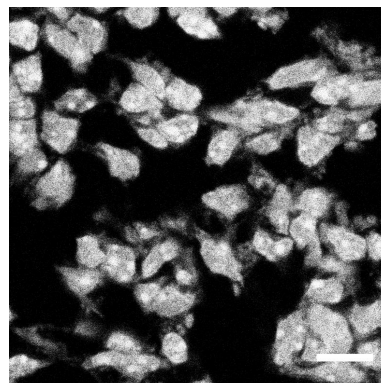


Control
Confocal: 0,88 µW ; 633nm
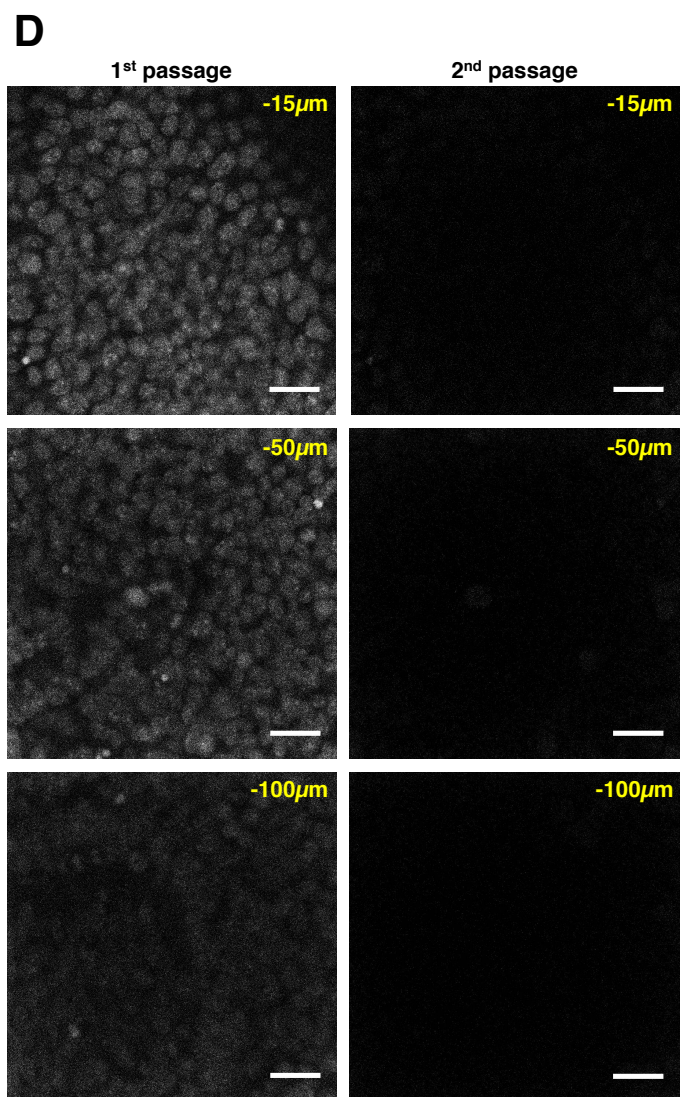
RTF
Confocal: 17,6 µW ; 633nm

# Figure 2

**A**

-30μm

1

2

1

-65μm
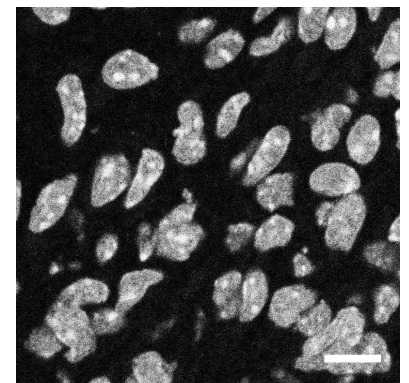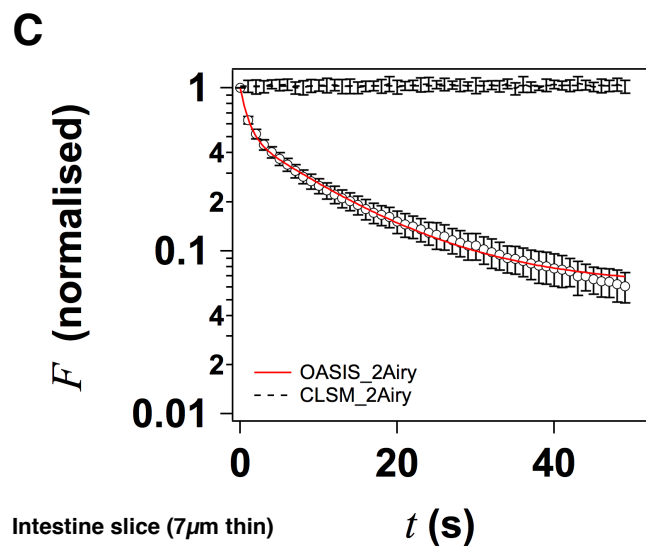
2

Control (*z*)
OASIS: 626 mW ; 15,7 mW/spot ; 760nm

**B**

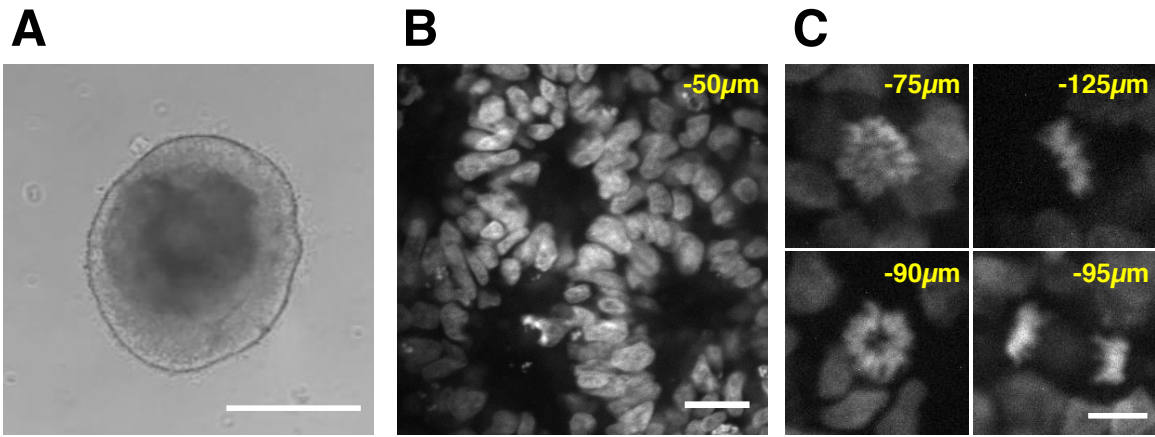-32μm

1

1

2

-115μm

2
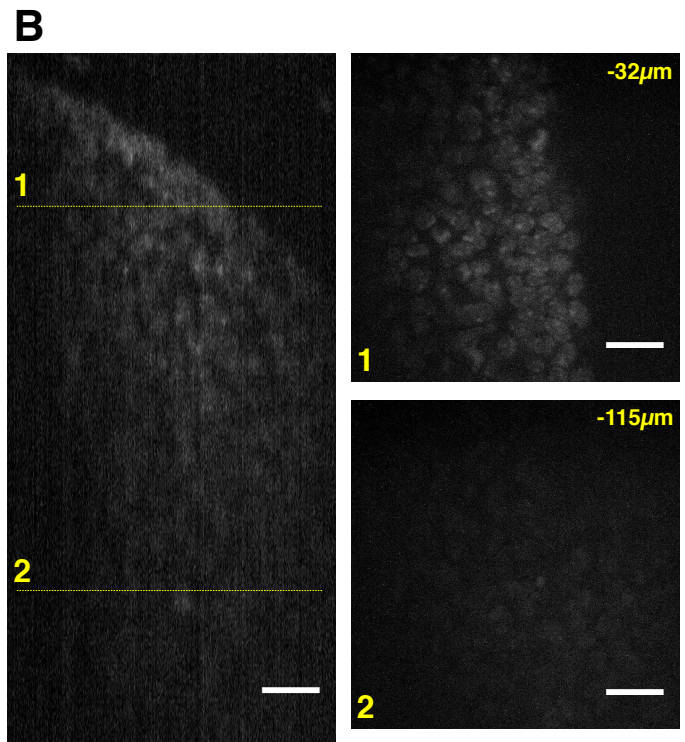
RTF (*xy*)
OASIS: 626 mW ; 15,7 mW/spot ; 760nm

**C**

OASIS_2Airy
CLSM_2Airy

$t$ **(s)**

Intestine slice (7μm thin)

OASIS_2Airy
CLSM_2Airy

Embryo (30μm depth - OASIS)

**#** **(scan)**

**D**

1$^{st}$ passage

2$^{nd}$ passage

-15μm

-15μm

-50μm

-50μm

-100μm

-100μm
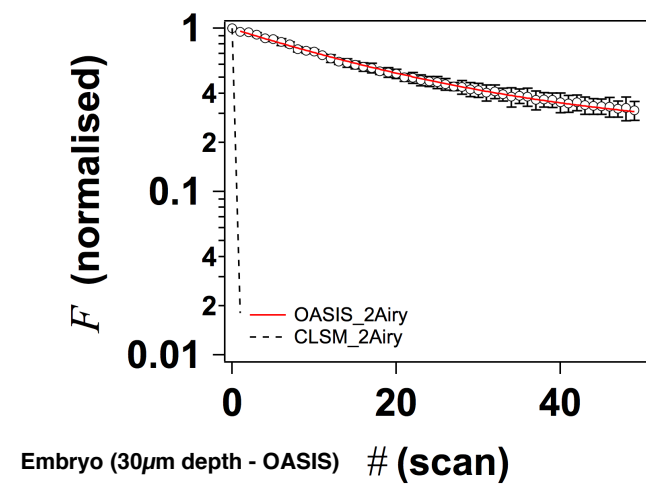
Control (*xy*)
Confocal: 9,36 ; 15,6 ; 26 μW ; 633nm

**Figure 3**

**A**

Control (xy)
Macroscope

**B**

-50µm

RTF (xy)
OASIS: 616 mW ; 15,4 mW/spot ; 760nm

**C**

-75µm    -125µm

-90µm    -95µm

RTF (xy)
OASIS: 616 mW ; 15,4 mW/spot ; 760nm

**D**

1

2

3

#
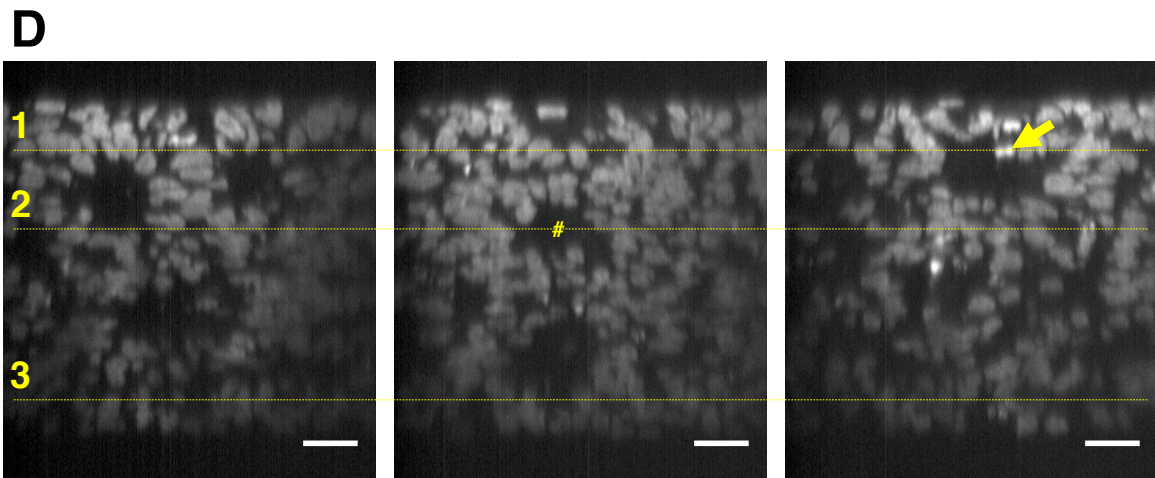
RTF (z)
OASIS: 630 mW ; 15,7 mW/spot ; 760nm

**E**

1    -42µm

2    -75µm

#

3    -155µm
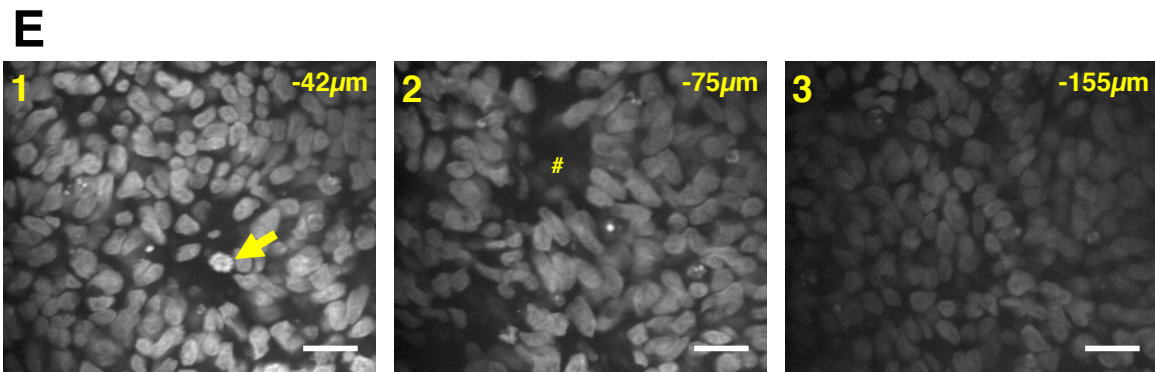
RTF (xy)
OASIS: 630 mW ; 15,7 mW/spot ; 760nm

**Figure 4**

**A**



Control (xy)
Macroscope

**B**



-45μm

RTF (xy)
OASIS: 614 mW ; 15,4 mW/spot ; 760nm

**C**



1
2
3

1  -30μm
2  -80μm
3  -125μm

RTF (z)
OASIS: 614 mW ; 15,4 mW/spot ; 760nm

**D**



1
2
3

1  -20μm
2  -35μm
3  -75μm

RTF (z)
OASIS: 614 mW ; 15,4 mW/spot ; 760nm

**Figure 5**